van Zalinge, M. E., Cashman, K. V., & Sparks, R. S. J. (2018). Causes of fragmented crystals in ignimbrites: a case study of the Cardones ignimbrite, Northern Chile. *Bulletin of Volcanology*, *80*(3), [22]. https://doi.org/10.1007/s00445-018-1196-2

University of Bristol - Explore Bristol Research
General rights

CrossMark

Causes of fragmented crystals in ignimbrites: a case study of the Cardones ignimbrite, Northern Chile

M. E. van Zalinge[1] · K. V. Cashman[1] · R. S. J. Sparks[1]

Abstract

Broken crystals have been documented in many large-volume caldera-forming ignimbrites and can help to understand the role of crystal fragmentation in both eruption and compaction processes, the latter generally overlooked in the literature. This study investigates the origin of fragmented crystals in the > 1260 km^3, crystal-rich Cardones ignimbrites located in the Central Andes. Observations of fragmented crystals in non-welded pumice clasts indicate that primary fragmentation includes extensive crystal breakage and an associated ca. 5 vol% expansion of individual crystals while preserving their original shapes. These observations are consistent with the hypothesis that crystals fragment in a brittle response to rapid decompression associated with the eruption. Additionally, we observe that the extent of crystal fragmentation increases with increasing stratigraphic depth in the ignimbrite, recording secondary crystal fragmentation during welding and compaction. Secondary crystal fragmentation aids welding and compaction in two ways. First, enhanced crystal fragmentation at crystal-crystal contacts accommodates compaction along the principal axis of stress. Second, rotation and displacement of individual crystal fragments enhances lateral flow in the direction(s) of least principal stress. This process increases crystal aspect ratios and forms textures that resemble mantled porphyroclasts in shear zones, indicating lateral flow adds to processes of compaction and welding alongside bubble collapse. In the Cardones ignimbrite, secondary fragmentation commences at depths of 175–250 m (lithostatic pressures 4–6 MPa), and is modulated by both the overlying crystal load and the time spent above the glass transition temperature. Under these conditions, the existence of force-chains can produce stresses at crystal-crystal contacts of a few times the lithostatic pressure. We suggest that documenting crystal textures, in addition to conventional welding parameters, can provide useful information about welding processes in thick crystal-rich ignimbrites.

Keywords Ignimbrite · Crystal · Fragmentation · Deformation · Welding · Compaction

Introduction

Broken crystals are characteristic of the products of explosive eruptions, particularly pyroclastic density current deposits (i.e. ignimbrites; ash-flow tuffs) associated with large caldera-forming eruptions. Ignimbrites with broken crystals include: many in the Great Basin, USA (Best and Christiansen 1997 and references therein); the Fish Canyon Tuff, USA (Lipman et al. 1997); the Cerro Galan ignimbrite, Argentina (Wright et al. 2011); Bishop Tuff, USA (Pamukcu et al. 2012; Bindeman 2005); the Huckleberry Ridge Tuff, USA (Bindeman 2005); the Ora ignimbrite, Italy (Willcock et al. 2015); and the Cardones ignimbrite, Chile (van Zalinge et al. 2016a). Broken crystals have also been documented in smaller explosive eruptions (Bindeman 2005; Williamson et al. 2010) and lavas (e.g., Allen and McPhie 2003; Cordonnier et al. 2009).

Understanding the origin of broken crystals in volcanic deposits can be challenging as several processes within the magmatic-volcanic system can fragment crystals. Magma, especially crystal-rich magma, can respond brittlely to rapid stress perturbations in magmatic systems (e.g. Spieler et al. 2004; Lavallée et al. 2007; Gottsmann et al. 2009; Huber et al. 2011; Jones et al. 2016). Magma decompression also causes over pressurisation and explosion of melt inclusions trapped in phenocrysts (Tait 1992; Best and Christiansen 1997; Zhang 1998; Williamson et al. 2010). Heating experiments show

✉ M. E. van Zalinge
m.vanzalinge@bristol.ac.uk

[1] School of Earth Sciences, University of Bristol, Wills Memorial Building, Queens Road, Clifton, Bristol BS8 1RJ, UK

melt inclusions can decrepitate when overpressures are generated by heating, and hence, crystals may fragment during episodes of magma recharge (Bindeman 2005). Crystals may also break during syn-eruptive processes, which include shearing of magma along the conduit margin (Polacci et al. 2001; Rosi et al. 2004; Cordonnier et al. 2009) and mutually impacting crystals in the magma (Best and Christiansen 1997; Cashman et al. 2008). Further fragmentation can occur during turbulent flow of fragmented particles in conduits and during transport in pyroclastic density currents (PDCs). Whilst it is thus clear that pre-and syn-eruptive processes play a significant role in crystal fragmentation, comparatively little attention has been paid to the response of crystals to post-eruptive processes such as welding and compaction of ignimbrites.

Welding of ignimbrites occurs by loss of void space during compaction due to loading, accompanied by volatile resorption in the matrix and pumice glass, as well as sintering of hot glassy material (Smith 1960; Sparks et al. 1999). These processes are controlled by the residence time of the pyroclastic material above the glass transition temperature, the deposit thickness, the compactional load (Smith 1960; Riehle et al. 1995; Quane and Russell 2005; Wright and Cashman 2014) and rates of volatile absorption by glass components (Sparks et al. 1999). The degree of welding can be quantified by measuring the density and porosity of the matrix, the aspect ratios of pumice clasts (fiamme), and the deformation of glass shards (e.g. Peterson 1979; Quane and Russell 2005; Wright and Cashman 2014). Despite the large literature on welding and compaction of ignimbrites, however, there are no studies of crystal deformation during compaction.

Theoretical and experimental studies of the rheology of crystal-melt suspensions indicate that touching crystal networks can form at ≤25 vol% crystals, depending on crystal shape and orientation (Saar et al. 2001; Hoover et al. 2001; Walsh and Saar 2008). Where uniaxial compression is applied to a crystal-bearing (> 40 vol% crystals) melt, crystal fracturing can occur where crystals are in contact (Lejeune and Richet 1995; Cordonnier et al. 2009). In such systems, stresses are typically distributed heterogeneously and most of applied force is supported in touching networks, or 'force-chains' (Mueth et al. 1998; Blair et al. 2001). We suggest that these concepts have important implications for crystal fragmentation and deformation during welding of large-volume crystal-rich ignimbrites, where deposit thicknesses of hundreds of meters create lithostatic stresses < 20 MPa. Such high pressures can completely eliminate the porosity in the deposit and therefore increase the bulk volume percentage of the crystals, which may exceed > 25 vol% (e.g. van Zalinge et al. 2016a). These crystallinities are sufficient to form crystal frameworks (force-chains; e.g., Liu and Nagel 2010) and promote crystal fragmentation and deformation. In such systems, local stresses at crystal contacts in force-chains are expected to exceed the average (lithostatic) pressure by a factor proportional to the

contact area of the touching crystal network (e.g., Walsh and Saar 2008), so that local stresses can exceed compressive strengths and crush crystals.

This study aims to unravel the multiple and complex processes of pre-, syn-and post-eruption fragmentation in the 'super' eruptions that form large ignimbrites. Our case study is the 21.9 Ma Cardones ignimbrite, which contains abundant broken phenocrysts (van Zalinge et al. 2016a). We document and analyse crystal textures in both pumice clasts and the bulk ignimbrite, and introduce a set of parameters to quantify the degree of crystal fragmentation (breaking a crystal into smaller fragments) and deformation (modification of the original euhedral crystal shape). The analyses are interpreted in the context of stratigraphic information on the Cardones ignimbrite previously published by van Zalinge et al. (2016a).

Geological and stratigraphic background

The Cardones ignimbrite is part of the early Miocene Oxaya Formation, which comprises at least four ignimbrites that together have a volume of ca. 3000 km³ and cover an area of ca. 42,000 km² on the Western Andean Slope in northernmost Chile and southernmost Peru (Fig. 1a; Wörner et al. 2000; García et al. 2004). In the mid to late Miocene, the Oxaya Formation was faulted and folded in the large-wavelength anticlines, creating elevations of ≤4000 m (van Zalinge et al. 2016a, b). A set of drill holes through the Oxaya Formation in northernmost Chile (Fig. 1a) allows detailed reconstruction of the ignimbrite sequence (van Zalinge et al. 2016a). The dominant member in the drill holes is the extra-caldera outflow sheet of Cardones ignimbrite, which has thicknesses of 300–1200 m. The associated caldera of this ignimbrite has not been identified, but must have been located to the east of the study area.

The Cardones ignimbrite can be divided into two Units—Unit 1 and Unit 2—using stratigraphic breaks and welding profiles (Fig. 1b; Van Zalinge et al. 2016a). In this study, we focus on the oldest, thickest and best-preserved Unit 1, which consists of four gradational subunits (subunit 1 to subunit 4) distinguished by their pumice and lithic contents (Fig. 1b). The thickness of the two basal subunits varies laterally and reflects the rugged pre-eruptive topography (a paleo-slope dissected by river valleys) that was inundated by the Cardones ignimbrite (van Zalinge et al. 2016b). The full stratigraphy of Unit 1 is well preserved in drill holes 7, 2, 4, 6 and 9, where Unit 1 is covered by younger ignimbrite members of the Oxaya Formation. At the hinge of the anticline (holes 1, 5 and 3), in contrast, erosion of Unit 1 accompanied relief generation in the Miocene. By extrapolating the non-welded surface of the Cardones ignimbrite from both limbs of anticline towards the hinge, the maximum pre-erosion thickness in holes 1 and 5 was reconstructed to be 1190 and 770 m, respectively (van Zalinge et al. 2016b). The pre-eroded thickness
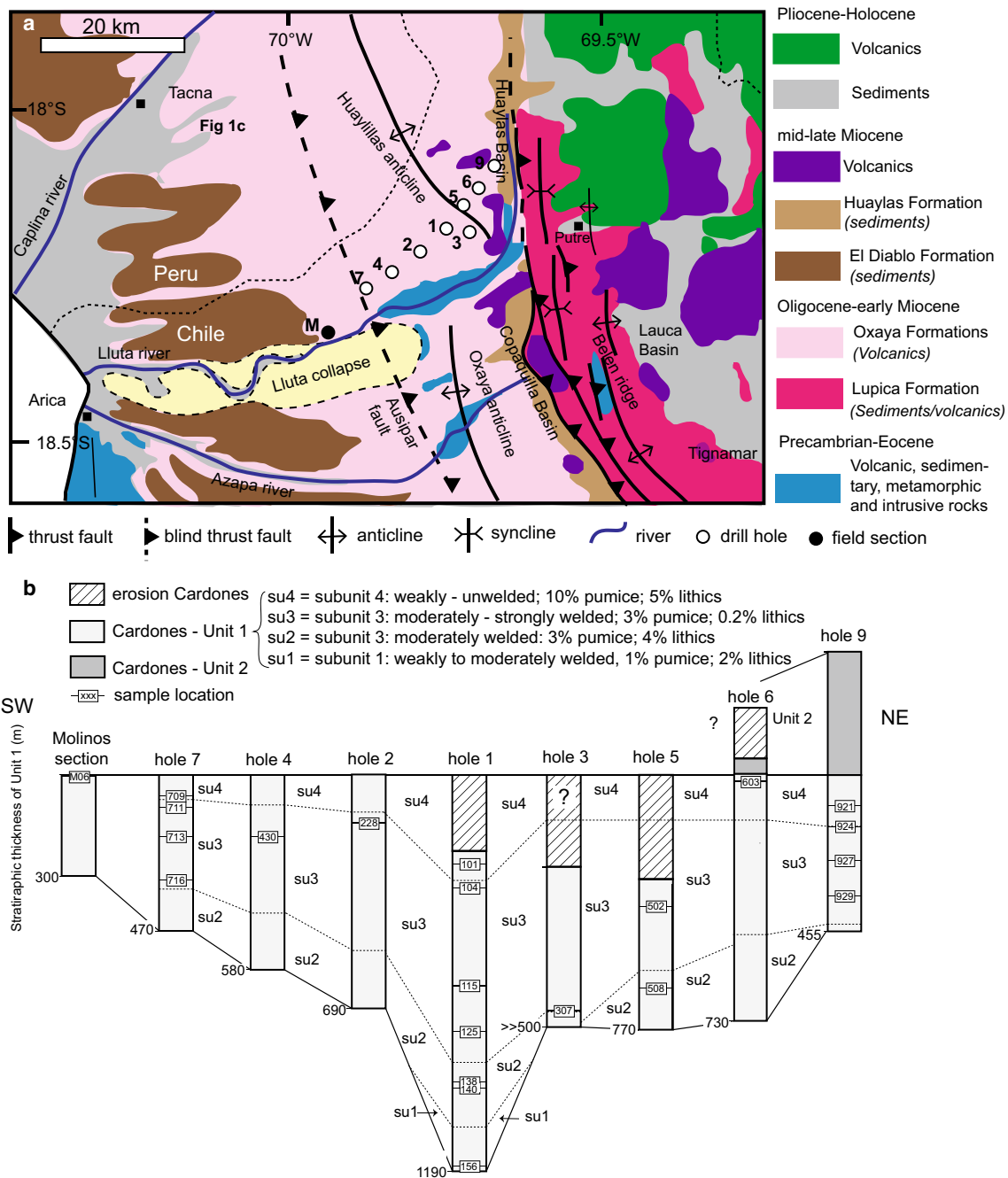
Fig. 1 **a** Simplified geological map of northernmost Chile and southernmost Peru (modified after García et al. 2011) with the locations of drill holes and the Molinos field section (M). **b** Stratigraphy of the Cardones ignimbrite based on van Zalinge et al. (2016a) with sample locations

of the Unit 1 in hole 3 is unknown, but the lack of a non-welded top indicates that the full thickness must have been > 500 m.

The bulk ignimbrite of Unit 1 contains 23–52 vol% crystal fragments (41 ± 9 (1σ)) that float in a devitrified matrix. This unit also contains 1–10% pumice that can be divided into ca. 80% crystal-rich pumice clasts (Fig. 2a) and ca. 20% crystal-poor pumice clasts (Fig. 2b, c). These two pumice types are chemically indistinguishable but texturally different (van Zalinge et al. 2016a, 2017). Modal analyses indicate that the

crystal-rich pumice contains 26–56 vol% (average 37 ± 8 (1σ)) crystals with an assemblage of plagioclase + quartz ± sanidine + biotite + titanomagnetite ± amphibole. In these clasts, most crystals are fragmented, but the original euhedral crystal outlines are still recognisable. In contrast, crystal-poor pumice clasts contain ca. 22 vol% crystal fragments and evidence of original crystal shapes is absent. The crystal fragments are typically < 1 mm in size and are angular to subrounded in shape.
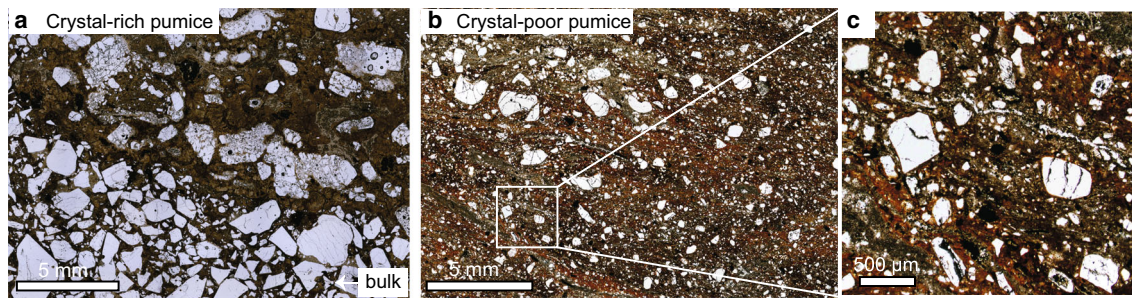
Fig. 2 Petrographic images of crystal-rich pumice and bulk ignimbrite (bulk) (**a**) and crystal-poor pumice (**b**, **c**). Note that the crystal fragments in the crystal-rich pumice outline original crystal shapes, whereas angular to sub-rounded fragments are free-floating in the crystal-poor pumice

Samples and methods

To investigate crystal textures and to unravel the multiple stages of fragmentation and deformation, we studied polished thin sections of crystal-rich pumice clasts with a petrographic microscope. Most thin sections are oriented in the (vertical) xz-plane, in which the z-axis is parallel to the highest principle stress (σ_1) applied by the compactional load. We then compared our results to observations of the bulk ignimbrite, which is the greater part of the ignimbrite and is dominated by crystal fragments in a devitrified matrix.

We analysed crystal textures of quartz and feldspar (plagioclase and sanidine) in crystal-rich pumice, with a specific emphasis on crystal breakage patterns (fragmentation). Sample locations and details are indicated in Fig. 1b and Table 1

respectively. We define a fragmented crystal as a region containing broken pieces that originally formed one single crystal (Fig. 3). In some cases, these fragments still outline the "original euhedral crystal shape"; with this term, we mean the shape of the crystal prior to fragmentation. Individual crystals are identified by their monomineralic nature, the proximity of crystal fragments and, in feldspar, by common zoning patterns (Fig. 3a). In the more extreme cases, individual crystals are identified by the occurrence of discrete fragment clusters (Fig. 3c). For practical reasons, we quantified crystal breakage by classifying individual crystals as (1) unbroken, (2) crystals broken into 2–25 fragments and (3) crystals broken into > 25 fragments.

A broken crystal either closely preserves the original crystal shape (Fig. 3a) or shows various degrees of fragment displacement and rotation (Fig. 3b, c). To determine the original

Table 1 Overview of pumice samples. Data on crystal content from van Zalinge et al. (2016a, 2017). Drill cores that experienced erosion of Unit 1 are indicated with an asterisk and for these samples we provide a stratigraphic depth range. The minimum depth is found when not taking

erosion into account and the maximum depth is found by taking the reconstructed thickness for Unit 1 (van Zalinge et al. 2016b). Lithostatic pressure calculated using a density of 2300 kg/m³

Sample	Orientation thin section	Subunit	Crystal content pumice (vol%)	Stratigraphic depth Unit 1 (m)	Lithostatic pressure (MPa)	Number of analysed feldspar	Number of analysed quartz
M06	random	Subunit 4	34.8	0	0	20	19
603	xz-plane	Subunit 4	26.6	20	0.5	18	6
711	xz-plane	Subunit 3	31.6	94	2.1	18	14
228	xz-plane	Subunit 3	36.8	143	3.2	26	14
101	random	Subunit 4	56.2	36–281*	0.8–6.3	24	8
924	xz-plane	subunit 4/3	31.8 / 52.5	176	4.0	21	9
713	xz-plane	Subunit 3	36.0	181	4.1	19	4
430	random	Subunit 3	41.2	192	4.3	26	20
104	xy-plane	Subunit 3	30.7	105–350*	2.4–7.9	15	–
502	xz-plane	Subunit 3	37.2	89–407*	2.0–9.2	26	14
716	xz-plane	Subunit 3	45.9	314	7.1	26	14
929	xz-plane	Subunit 3	26.6 / 33.7	361	8.1	13	9
508	xz-plane	Subunit 2	35.5	333–651*	7.5–14.7	26	17
307	xz-plane	Subunit 3/2	332.5	> 500	> 11.2	26	21
125	random	Subunit 3	33.3	537–782 *	12.1–17.6	15	6
138	xz-plane	Subunit 2	39.0	681–926 *	15.4–20.9	12	14
140	xy-plane	Subunit 2	34.0	696–941 *	15.7–21.2	14	14
156	xz-plane	Subunit 1	40.7	922–1167 *	20.8–26.3	26	9

size of unbroken and moderately fragmented crystals, we identified all crystal fragments and measured the apparent long axis of the collective fragments (Fig. 3a, b). However, crystal deformation increases the original long axis of the crystals and thus estimates of original crystal length were limited to crystals that show limited deformation. To quantify rotation, we recorded observations of extinction angles in crossed polarised light (xpl; Fig. 3). It is clear from the hand samples and the thin sections oriented in the vertical (xz-)plane that crystal fragments are often also displaced in

the horizontal (xy-)plane, (Fig. 3c). We measure displacement as the aspect ratio of individual crystals (including all associated crystal fragments) in thin section, calculated by dividing the maximum length of the fragmented crystal in the horizontal plane by the maximum width of the fragmented crystal in the vertical plane. In this way we quantify the fragment displacement perpendicular to the highest stress (σ_1) applied by the compactional load. Where thin sections were not oriented in the xz-plane, the measured aspect ratios provide minimum estimates of deformation (Table 1).

Fig. 3 Plane polarised light (ppl) and crossed polarised light (xpl) petrographic images of quartz (left) and feldspar (right) crystals in crystal-rich pumice clasts. **a** In situ broken crystals where the fragments show minor displacement and original crystal shapes are still discernable. **b** Original crystal shapes are slightly disturbed as some crystal fragments are displaced. Enhanced crystal fragmentation occurs where fragments are in contact (white arrows). **c** Complete destruction of crystal shape and fragments are smeared out horizontally, increasing the length and decreasing the width of the crystal. Black arrows in the ppl images indicate the apparent long axis of the crystal used to measure the size. In the xpl images we indicated the length and width of the crystal, used to measure the aspect ratio. Black arrows at the left side of (**b**) and (**c**) point upwards in the stratigraphy
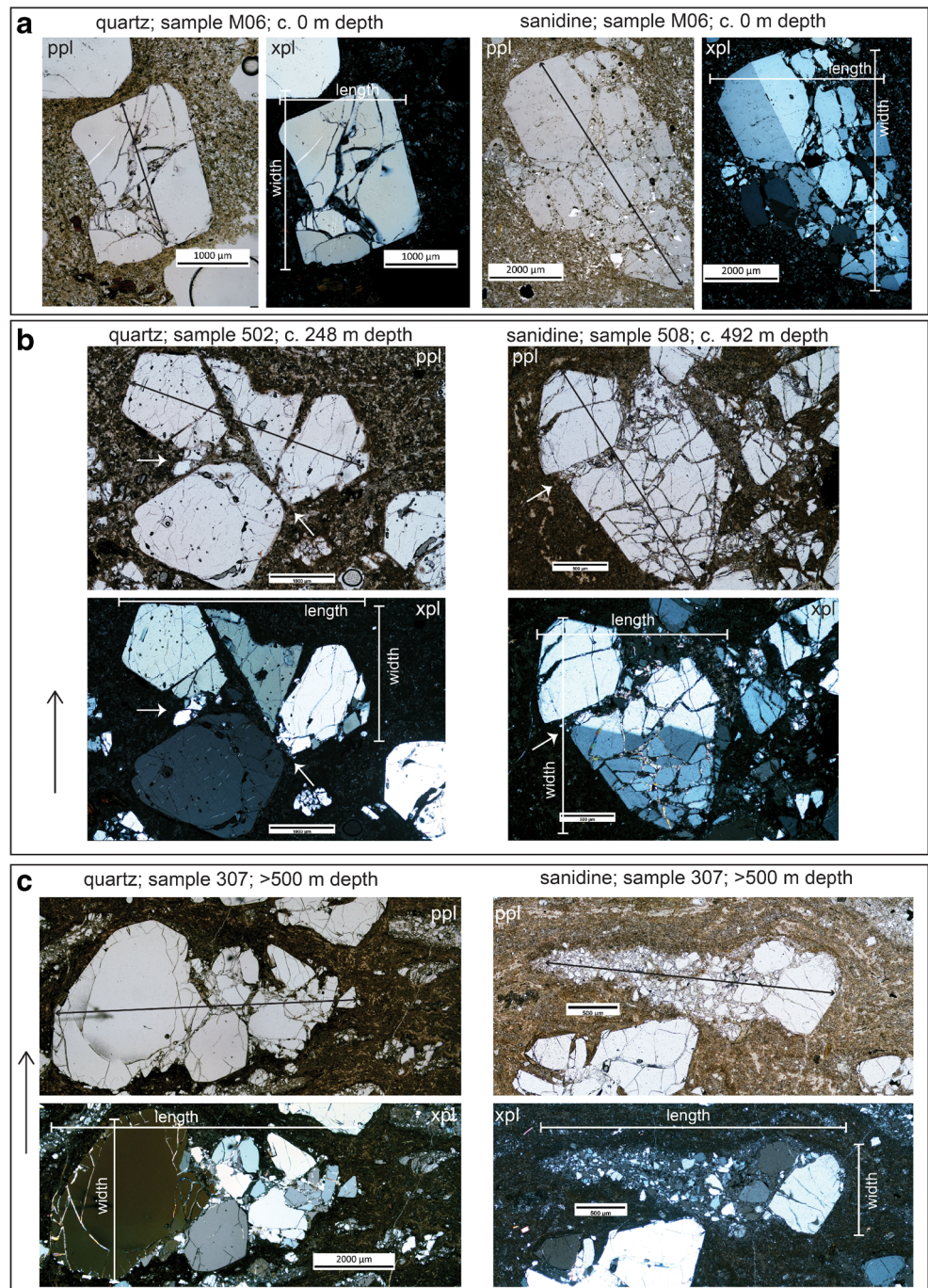
To calculate expansion accompanying fragmentation, we measured the space between the fragments of the same crystal (that is, the dilated volume of individual crystals) from high-resolution petrographic images. This was possible only where the original crystal shape could still be discerned (e.g. Fig. 3a, b). We first created a set of binary images using the software ImageJ (Rasband 1997). We then used the binary images to compare the broken crystal area (including interior gaps, which were either empty or filled with devitrified glass and/or secondary minerals) to the combined area of the crystal fragments (that is, the pre-breakage crystal area).

Results

Pumice clasts in the Cardones ignimbrite contain phenocrysts that are fragmented and variably deformed. Here, we summarise metrics of fragmentation extent and timing, as well as post-fragmentation deformation, as a function of location (stratigraphic depth) within the ignimbrite. We then compare crystal breakage textures within pumice clasts to those preserved within the bulk ignimbrite.

Number of crystal fragments

The simplest measure of fragmentation is the number of crystal fragments. In general, this number increases with stratigraphic depth within Unit 1. Specifically, in pumice clasts sampled at depths greater than ca. 180 m (from sample 713 onwards; Fig. 1b), crystals comprising > 25 fragments are more abundant than in pumice clasts higher in the stratigraphy (Fig. 4a, b). Quartz crystals are less broken than feldspar, as measured both by the percentage of unbroken crystals and the frequency of highly fragmented crystals (> 25 fragments). The observed difference between quartz and feldspar is commensurate with quartz being stronger than feldspar, where fracturing is controlled by cleavage planes (Evans 1988).

Fragmentation efficiency, measured by the number of fragments per crystal, is related to crystal size. In general, smaller crystals are less broken than larger crystals, as illustrated in Fig. 4c. Here, the data for the uppermost six pumice samples (< 180 m) are plotted separately from those of deeper pumice to highlight the increase in fragmentation efficiency with depth. Importantly, the relationship between the number of fragments per crystal and the crystal size explains the scatter Fig. 3a, b. For example, samples 125 and 929 (black arrows in Fig. 3a, b) contain large numbers of small crystals compared to the other samples, and thus, the percentages of unbroken and minimally broken crystals are also relatively large.

The bulk ignimbrite contains crystal fragments that are floating in a devitrified matrix. In contrast to the crystals in pumice clasts, broken pieces that originally formed one single crystal are no longer found in close proximity in the matrix

Fig. 4 **a**, **b** Stacked bar charts indicating number of fragments and the ▶ crystal size per sample for feldspar (**a**) and quartz (**b**). Samples are ordered with increasing stratigraphic depth (*average depth from the range given in Table 1). **c** One hundred percent stacked column charts indicating the number of fragments per crystal-size group. The uppermost six samples are plotted separate from the deeper samples, indicating smaller crystals are less broken than larger crystals

(Fig. 5). This observation indicates that the fragmented crystals within the bulk ignimbrite are completely dismembered during eruption and that the fragments are thoroughly mixed during transport within PDCs. In situ crystal breakage is observed (white arrows in Fig. 5) where individual crystal fragments are touching. Here, fragmentation by crystal-crystal interaction can be seen either where two crystal fragments (Fig. 5a) are in contact or where a (weaker) third fragment is crushed between two fragments (Fig. 5b). We see similar evidence for this additional stage of fragmentation within individual pumice clasts at stratigraphic depths > 180 m, where intense fragmentation is also observed where two fragments are in contact with one another or where there are intervening weaker fragments (white arrows, Fig. 3b).

Arrangement of crystal fragments

In pumice clasts, fragments of a single broken crystal can be arranged in different ways. A crystal may be broken without displacing individual fragments, in which case the original euhedral crystal shapes are still clearly recognisable (Fig. 3a). In cross-polarised light, the extinction angle of these crystal fragments is similar, as are the original patterns of twinning and zoning in feldspar crystal fragments is still recognisable; both observations indicate only minor rotation of the individual fragments. This type of fragmented, but undisrupted crystal, is common in pumice clasts from the upper parts of the ignimbrite stratigraphy. Since these crystals show very limited crystal displacement in the horizontal plane (e.g. Fig. 3a), the aspect ratios of these crystals are low: in general, ≥ 75% of the crystals at depths above ca. 250 m have aspect ratios less than two (Fig. 6a).

At > 250 m, individual fragments of crystals show markedly different extinction angles (Fig. 3b), indicating that they have been displaced and rotated. In more extreme cases, crystal fragments form high-aspect ratio trails (Fig. 3c) and original crystal shapes may no longer be recognisable. In some cases, crystal fragments have been displaced in such a way that larger core fragments have smaller grained "wings" (Fig. 7a). Such post-fragmentation deformation can be measured by the aspect ratio. Figure 6a shows that at depths > 300 m (from sample 716 downwards), up to 70% of the fragmented feldspars and 35% of the fragmented quartz crystals have aspect ratios greater than two. Again, samples with anomalously small crystals (samples 929 and 125—black arrows in Fig. 6a) show smaller aspect ratios and are less broken (Fig. 4). Pumice clasts at depths of ≥ 300 m also show crystal
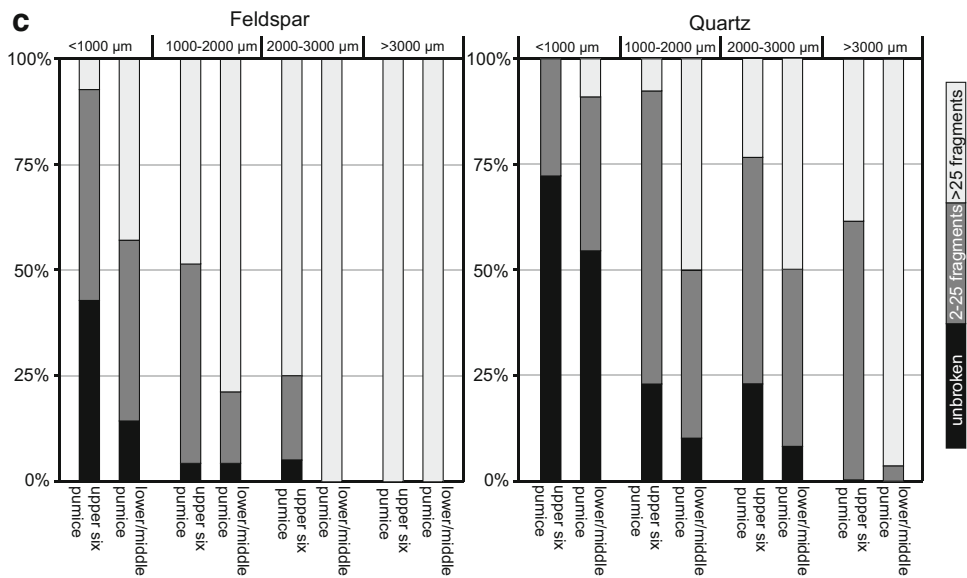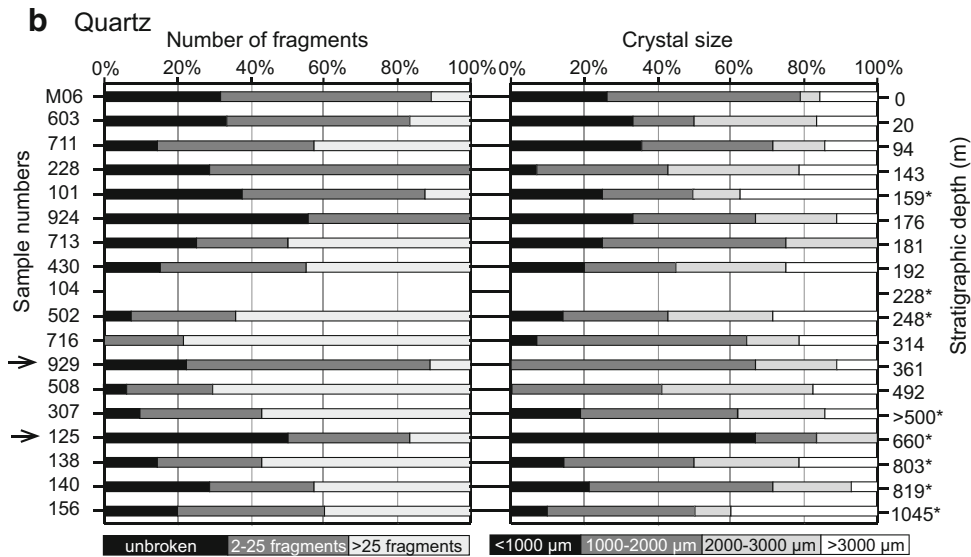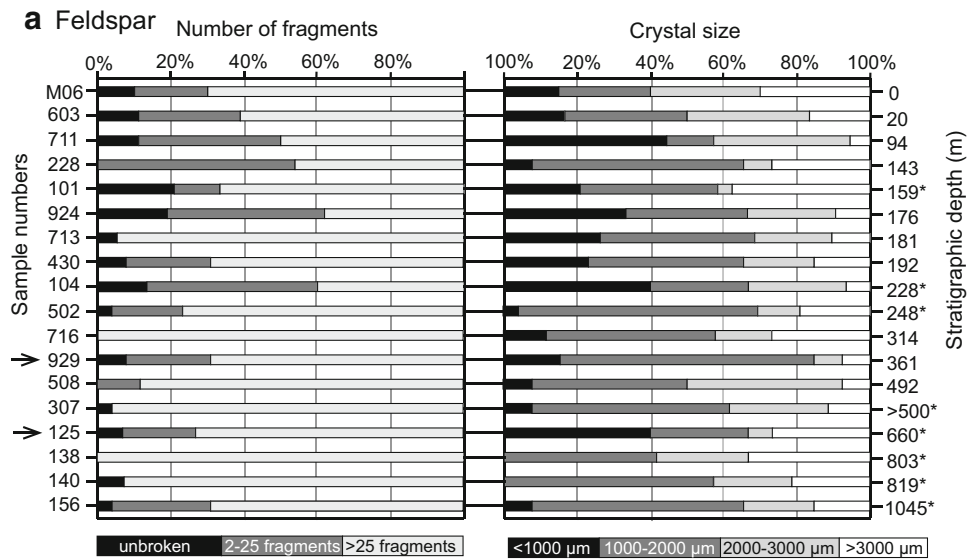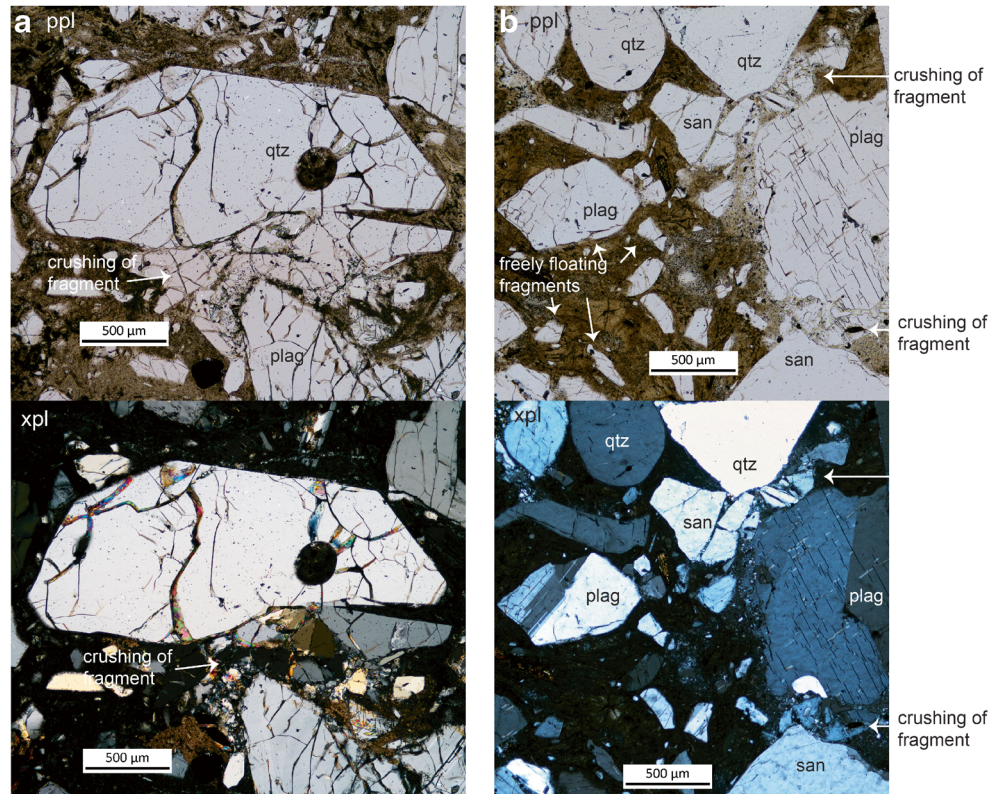
fragmentation and deformation of biotite and amphibole, as illustrated by a fragmented and bent biotite crystal (Fig. 7b) and a fragmented and extended amphibole (Fig. 7c).

We plotted data on fiamme aspect ratio and bulk ignimbrite density (van Zalinge et al. 2016a) alongside crystal aspect ratios

in Fig. 6a. In the uppermost ca. 200 m of the ignimbrite stratigraphy, crystal aspect ratios are typically less than two, although in this interval, fiamme aspect ratios progressively increase from two to four and the bulk ignimbrite density increases from < 1900 to 2300 kg/m^3. At stratigraphic levels > 200 m, bulk ignimbrite
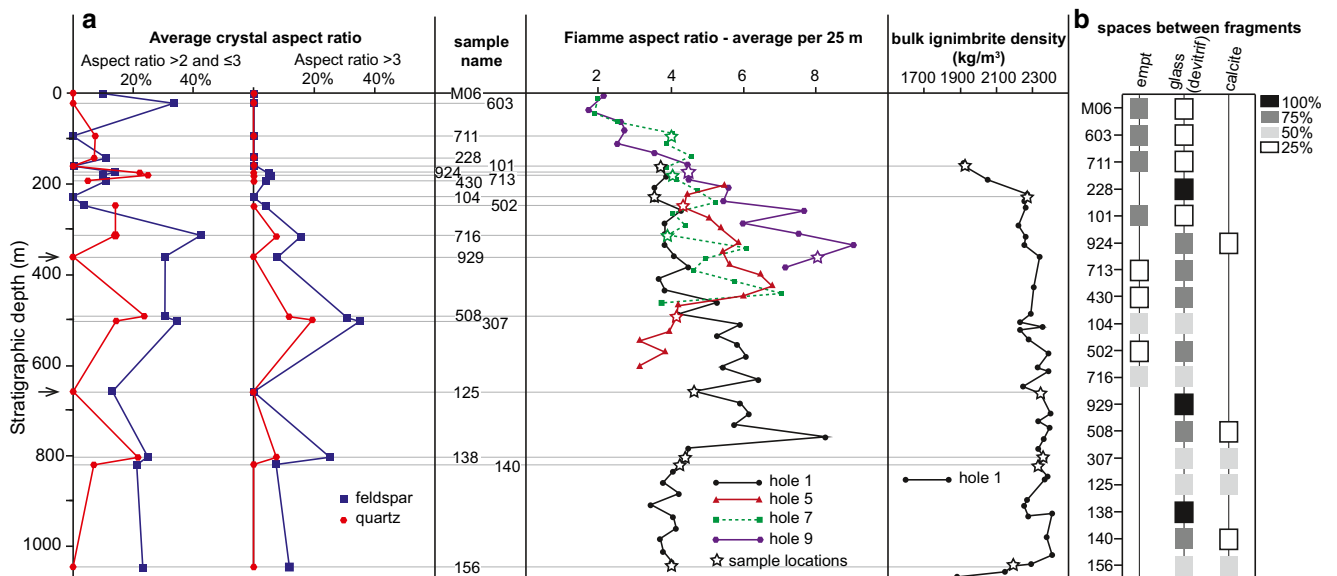
Fig. 6 a Percentage of crystals with an aspect ratio of (i) greater than two, (ii) less than or equal to three and (iii) greater than three, plotted against stratigraphic depth. Diagram also includes the average fiamme aspect ratio for selected holes and bulk ignimbrite density for hole 1 (data from van Zalinge et al. (2016a)). Fiamme aspect ratio data at the top of holes 1 and 5 are missing, because this part of the ignimbrite is eroded. **b** Diagram with estimated percentages of material in spaces between the crystal fragments

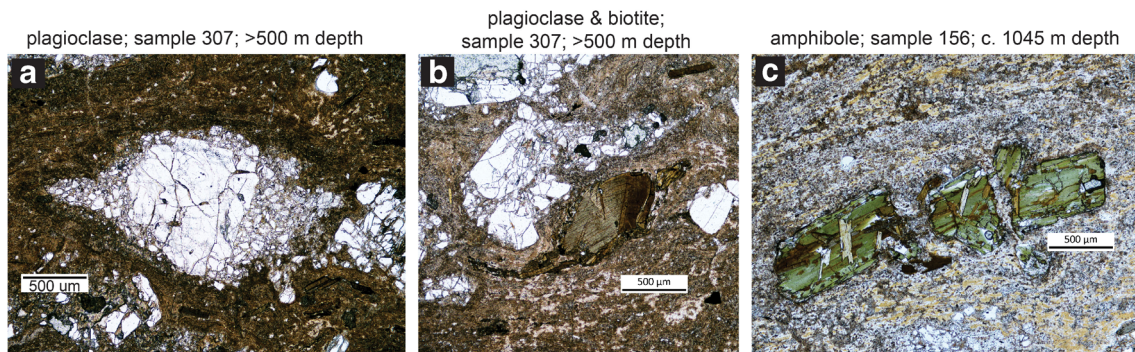**Fig. 7** Petrographic images of crystals in pumice, indicating evidence for shear (images are of a sample in the vertical sections). **a** Broken plagioclase resembling a φ-type porphyroclast. **b** Deformed plagioclase and biotite crystals, which both indicate evidence for rotation. **c** Amphibole crystal broken into fragments that are laterally displaced

density remains constant around 2300 kg/m³, while fiamme aspect ratios continue to increase with depth from four to seven (Fig. 6a). Crystal aspect ratios are also higher (greater than two) at depths > 200 m compared to crystal aspect ratios at the top of the ignimbrite (smaller than two). Patterns of deformation at the base of the ignimbrite vary with location. In holes 7 and 9, the mean aspect ratio rapidly decreases to three in the basal ca. 50 m. In holes 1 and 5, however, a more sudden decrease in the mean fiamme aspect occurs higher above the base, although this trend is not mimicked by either the bulk ignimbrite density or crystal aspect ratios.

Volume expansion accompanying eruption

Syn-eruption expansion of pumice is accommodated primarily by vesiculation of the melt. We note, however, that broken crystals in pumice clasts comprise fragments from the same crystal that do not touch, but instead are separated by a few tens to one hundred micrometres (Fig. 3a). We measured the space in between the fragments that belong to a single crystal, in ten crystals from the upper non-welded pumice clasts to determine volume percentage increase. For crystals broken into < 25 fragments, we estimated a dilated volume increase of 4 to 9%, with an average of 7% (n = 3). Extremely broken crystals (> 25 fragments) have a dilated volume increase of 13 to 58% (n = 7), with an average of 33%. For the latter group, the lower end of the range is probably most representative, as plucking of crystal fragments during sample preparation could have artificially increased the spaces between the fragments. Considering that a pumice clast contains unbroken, moderately broken and extremely broken crystals (Figs. 4a, b), we estimate that the average dilated space is about 12%. By combining the measured additional dilated space between the crystal fragments with the average crystal content of Cardones pumice (38 vol%), we estimate that ca. 5% space is created per pumice clast by primary fragmentation and expansion of the crystals.

The spaces between the fragments can be empty, or filled with (devitrified) glass, or secondary calcite (Fig. 6b). Empty spaces are especially common (in ca. 75% of the crystals analysed) in the uppermost pumice samples, with the remaining gaps filled with devitrified glass (25%). At depths greater than ca. 200 m, in contrast, the reverse is true, with glass- (melt-) filled spaces most common (ca. 75%). Pumice clasts from depths > 500 m may also contain 25–50% secondary calcite between crystal fragments. Calcite precipitation suggests that these gaps were originally open, and modal analyses by van Zalinge et al. (2017) indicate that when calcite is present in pumice clasts it ranges from 0.5 to 3 vol%.
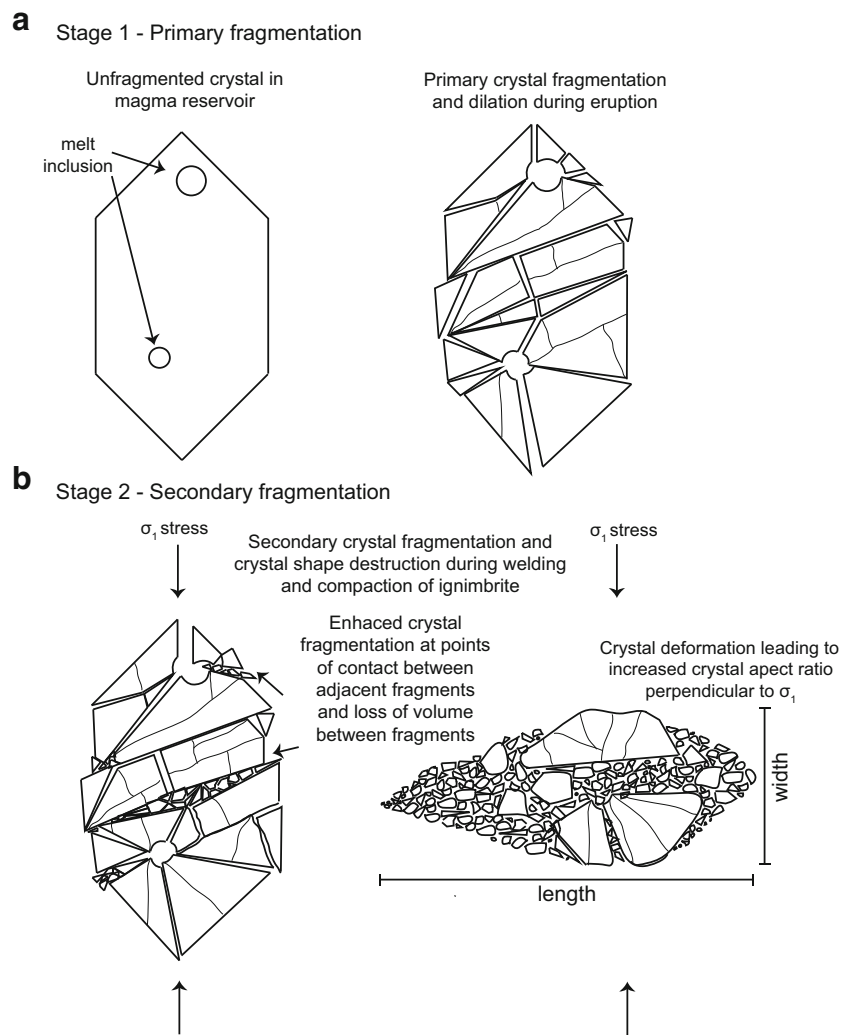
Discussion

Crystal textures indicative of fragmentation are ubiquitous throughout the Cardones ignimbrite. Stratigraphic variations in crystal textures, however, indicate that fragmentation occurs in two stages: primary syn-eruptive fragmentation and secondary post-eruptive fragmentation (Fig. 8).

Crystal textures related to primary syn-eruptive fragmentation are best observed in non-welded pumice clasts in the uppermost 200 m of the stratigraphy where secondary fragmentation is absent. Primary fragmentation is characterised by crystals that are broken, but with original crystal shapes that can still be discerned (Figs. 3a; Fig. 8a); this is reflected in their relatively low crystal aspect ratios (Fig. 6a). Here crystal fragments also show very little evidence for rotation or displacement, as measured by variations of extinction angles in cross-polarised light (Fig. 3a). The pumice clasts were transported tens of kilometres in PDCs prior to deposition. From this, we infer that the surrounding melt protected the fragmented crystals during eruption and emplacement, probably because of rapid cooling and glass formation. This interpretation is supported by evidence that the melt phase did not infill the spaces between the crystal fragments (Fig. 6b).

Secondary fragmentation becomes important at depths > 200 m, and is characterised by enhanced crystal fragmentation, often localised at points of contact between adjacent crystal fragments, as well as deformation of associated crystal

Fig. 8 Cartoons illustrate the two-stage crystal fragmentation process in the Cardones ignimbrite

a Stage 1 - Primary fragmentation

Unfragmented crystal in magma reservoir

melt inclusion

Primary crystal fragmentation and dilation during eruption

b Stage 2 - Secondary fragmentation

σ_1 stress

Secondary crystal fragmentation and crystal shape destruction during welding and compaction of ignimbrite

σ_1 stress

Enhaced crystal fragmentation at points of contact between adjacent fragments and loss of volume between fragments

Crystal deformation leading to increased crystal apect ratio perpendicular to σ_1

width

length

fragments (Fig. 8b). Crystal deformation is measured by the aspect ratios of the two most abundant phenocryst types, feldspar and quartz (Fig. 6a). Increasing aspect ratios of both phases with stratigraphic depth provide strong evidence for compaction-related deformation accompanying welding.

Primary fragmentation processes

Fragmentation of magma in explosive eruptions is widely thought to occur at threshold conditions, such as a critical vesicularity (Sparks 1978) or a critical strain rate (Papale 1999). In crystal-poor silicic melts, the critical vesicularity is estimated at 63–80% (Sparks 1978; Sparks et al. 1994; Gardner et al. 1996; Wright and Weinberg 2009; Lindoo et al. 2016), and is likely controlled by the relation between gas expansion and gas escape through permeable networks (e.g. Klug and Cashman 1996; Rust and Cashman 2011). In crystal-rich ignimbrites, the melt-based vesicularity is 50–75% (Bachmann et al. 2000; Lindsay et al. 2001; Wright et al. 2011). Although the upper boundary is comparable to that of crystal-poor pumice, the

lower end suggests that high crystal contents may alter critical vesicularity thresholds for fragmentation. One possible explanation is the effect of high crystal contents on the development of permeability in these samples, as illustrated by analogue (Oppenheimer et al. 2015) and high temperature (Lindoo et al. 2017) experiments. This fragmentation mechanism does not, however, explain the pervasive crystal fragmentation observed in large ignimbrite eruptions.

Primary fragmentation can be syn-eruptive (e.g. Best and Christiansen 1997) or pre-eruptive (e.g. Bindeman 2005). Very large ignimbrite eruptions may generate conditions that impose extreme pressure gradients (ΔP) within erupting magma, which may in turn affect fragmentation (e.g., Gottsmann et al. 2009; Cashman and Giordano 2014). For insight into the role of ΔP on fragmentation we look to experimental shock tube studies (e.g., Alidibirov and Dingwell 1996; Spieler et al. 2004; Mueller et al. 2008; Jones et al. 2016). Here magma fragmentation is caused by tensile fractures within the magma and occurs at a threshold ΔP with an efficiency determined by fracture strength and magma permeability. These studies show

that addition of crystals increases the bulk magma strength, but that the crystals may fracture if the pressure drop is large and rapid (e.g. Jones et al. 2016). An additional mechanism of crystal fragmentation is ΔP-induced explosion of crystal-hosted melt inclusions (e.g. Tait 1992; Best and Christiansen 1997; Williamson et al. 2010). Alternatively, melt inclusions may decrepitate by overpressures generated by heating if large eruptions are preceded by episodes of overheating (Bindeman 2005). Although variations in anorthite content and resorption textures in plagioclase crystals from the Cardones ignimbrite suggest pre-eruptive fluctuations in temperature, melt composition or water content (Van Zalinge et al. 2017), there is no evidence of inclusion decrepitation that results in the fragmentation of crystals in the magma reservoir. Moreover, it is difficult to imagine ways in which pre-broken crystals would survive eruption-triggered fragmentation without extensive disruption of the broken crystals. Instead, preservation of shapes that are close to the original crystal shape, together with a lack of evidence for post-fragmentation feldspar growth (e.g. Fig. 3), strongly supports that the primary fragmentation event was synchronous with eruption.

We suggest that the on average 12% dilated space between the crystal fragments was created during the eruption and is related to volatiles in melt inclusions coming out of solution, expanding and breaking the crystal. Such, isotropic crystal fragmentation by dilation pushes apart crystal fragments in all directions and suggests a very large pressure drop that exceeds the tensile strength of the crystals; shock tube experiments suggest that ΔPs of tens of MPa are required (Alidibirov and Dingwell 1996; Spieler et al. 2004; Mueller et al. 2008; Jones et al. 2016). Models of explosive volcanic flows in conduits calculate rapid ΔPs of this magnitude, with the largest and most rapid ΔPs occurring at and above the fragmentation level (decreases of several tens of MPa over ca. 10–30 s across the fragmentation level and during discharge into the atmosphere; Costa et al. 2009). The ΔP and rate (dP/dt) depend, moreover, on the conduit geometry, with the highest values occurring when a dyke feeds into a cylindrical conduit (Costa et al. 2009). One relevant observation here is that most of the Cardones ignimbrite has a low lithic content (< 5%; Fig. 1b). In models with fixed conduit geometries (either dykes or cylinders), very large underpressures developed in the conduit cause conduit erosion and high lithic contents. In contrast models with dykes feeding into cylindrical conduits do not develop large underpressures but maximise decompression rates, so this type of model is consistent with observations of the Cardones.

Crystal fragmentation accompanying syn-eruptive mush deformation

So far we have focused on crystal fragmentation in crystal-rich pumice clasts (Fig. 2a). Crystal-poor pumice clasts (Figs. 2b, c)

may also provide important additional information about crystal fragmentation and deformation processes. The crystal-poor pumice clasts account for 20% of all the pumice and contain only relatively small (<1 mm) angular to sub-rounded crystal fragments, indicating that the original crystals have been broken and completely dismembered, probably during eruption. Similar pumice types have been found in crystal-rich eruptions of Pinatubo, Philippines and Quilotoa, Ecuador (Polacci et al. 2001; Rosi et al. 2004). This pumice type has been interpreted as a response to extreme shearing of crystal-rich magma along feeder conduits during eruption, and that during this process the original crystals completely disintegrate. Van Zalinge et al. (2016a) proposed a similar interpretation for the crystal-poor pumice clasts in the Cardones ignimbrite, suggesting that syn-eruptive magma-shearing can also cause crystal fragmentation. Here, we introduce an alternative idea to the above. Following Cashman et al. (2017), van Zalinge et al. (2017) suggested the Cardones magmatic system contained at least two chemically distinct melt-dominated lenses (< 50 vol% crystals) embedded in a crystal-mush (> 50 vol% crystals) that destabilised and formed one large magma body shortly before eruption. We suggest that the crystal-rich mush could have been strongly deformed during this destabilisation event, creating extreme shear localisation. Deformation of a magmatic mush can cause mechanical instabilities, including shear zones (e.g. Petford 2003), which are most common in mush with low melt fractions (<25 vol% melt; Van der Molen and Paterson 1979; Rutter and Neumann 1995; Rushmer 1995; Paterson et al. 1998). Indeed, in experimentally deformed granites at magmatic temperatures with up to 25 vol% melt, shear is attained by crystal fracture accompanied by redistribution of melt into films perpendicular to the lowest stress (Van der Molen and Paterson 1979), and experimentally deformed granite with 10–40 vol% melt shows pervasive cataclastic crystal granulation and collapse of melt-filled pore space (Rutter and Neumann 1995). The presence of small, angular to sub-rounded crystal fragments in the crystal-poor pumice (Fig. 2c) is consistent with cataclastic granulation observed in these experiments. The lower crystal content of this highly sheared magma may also reflect melt extraction from the mush and migration into the weakened shear zones. The lack of crystal growth after crystal fragmentation indicates that this process must have been synchronous with the eruption. Hence, we speculate that the crystal-poor pumice in the Cardones ignimbrite could record mush deformation during destabilisation of a magma-mush system, rather than shear along the feeder conduit as previously suggested. Thus, this process can also contribute to crystal fragmentation during large caldera-forming "super" eruptions that produce large-volume ignimbrites.

Compaction-related secondary fragmentation

Our data show that crystals within pumice clasts are more fragmented and deformed at greater stratigraphic depths

(Figs 4 and 6a). In the upper ca. 200 m of the stratigraphy, crystals show evidence for only primary fragmentation (Fig. 8a). This primary fragmentation was accompanied by dilation, which provides space for fragments to rotate. Under compaction at depths > 200 m (ca. 5 MPa), this particle rotation allows secondary fragmentation by particle-particle interactions (Fig. 8b). In detail, secondary fragmentation initiates either at the contact point between two fragments or where two "stronger" fragments crush a third "weaker" fragment (Fig. 3b). The result is a pronounced increase in the number of fragments per crystal (Figs. 3b and 4a, b), and a corresponding decrease in fragment size (Fig. 8b). The same process is seen in bulk ignimbrite samples, where compaction causes secondary fragmentation by fragment-to-fragment interaction (Fig. 5).

To explain secondary fragmentation in the bulk ignimbrite and pumice clasts, we look to the behavior of crystal-rich materials, particularly creation of force-chains (e.g. Mueth et al. 1998; Blair et al. 2001). Percolation analysis shows that the formation of interconnected crystal networks depends on crystal shape, and that such networks start to develop at > 25 vol% crystals (Saar et al. 2001; Hoover et al. 2001); the high crystallinity of the Cardones bulk ignimbrite (on average 41 vol% crystals) and pumice clasts (on average 38 vol% crystals) thus guarantees that crystal networks are present. Clear evidence for crystal breakage at points of contact further shows that these support sufficient stresses imposed by the overlying ignimbrite to fragment crystals. Under conditions of uniaxial compression, individual crystals in crystal-rich dacite at magmatic temperatures can fracture at pressures ≥ 10 MPa (Lavallée et al. 2007; Cordonnier et al. 2009). However, we find evidence for pervasive secondary crystal fragmentation at lithostatic pressures of ca. 5 MPa. We suggest that the crystal networks in the Cardones ignimbrite act as force-chains that support most of the forces applied by the overlying ignimbrite load, where stresses can locally exceed the average applied force by six times (Mueth et al. 1998; Blair et al. 2001). The presence of force-chains also explains the heterogeneous character of crystal fragmentation in pumice clasts and bulk ignimbrite.

Based on our observations, we can conclude that, in thick (> 200 m) crystal-rich ignimbrites (> 30%), secondary crystal fragmentation related to welding compaction plays an important role. However, the ductile deformation of the glassy matrix in pumice and bulk ignimbrite is crucial to facilitate secondary fragmentation and deformation of the rigid crystals. Using the bulk ignimbrite density, van Zalinge et al. (2016a) calculated that welding of the matrix (at depths greater than ca. 200 m) was associated with complete elimination of the ca. 30% porosity. Reduction of matrix porosity increases the relative abundance of crystals and thus promotes formation of connected crystal frameworks. The observation that secondary fragmentation becomes particularly prevalent at depths > 200 m (Fig. 6a) suggests that porosity reduction in both pumice and bulk ignimbrite matrix

is necessary for secondary fragmentation. Hence, we suggest that brittle secondary fragmentation of crystals follows the ductile deformation of the glassy matrix. It is not as clear when secondary fragmentation ceases, but once the matrix reaches the glass transition temperature, the crystals are not the only rigid objects, and the glass will also fail. As we did not find evidence for large-scale brittle deformation of the glass, it appears that secondary crystal breakage ceases when the melt reaches the glass transition temperature. At this point the stresses will be more uniformly distributed through the ignimbrite. Following the model of Riehle et al. (1995), we would expect the middle section of the ignimbrite to have had a longer time above the glass transition temperature than the base and top, and thus we would expect to see more extensive secondary fragmentation. Indeed, both the fragmentation efficiency (Fig. 4) and the extent of post-fragmentation crystal deformation (Fig. 6a) are highest in this region, which also is characterised by glass matrix in the spaces between the crystals fragments (Fig. 3b, c).

To summarise, we propose that secondary crystal fragmentation aids welding and compaction in two ways. First, enhanced crystal fragmentation at crystal-crystal contacts deforms those boundaries to accommodate compaction along the principal axis of stress. Second, rotation and displacement of individual crystal fragments enhances lateral flow in the direction(s) of least principal stress, producing elongate "trails" of fine particles, often around larger core pieces of the original crystal (Figs. 3c and 7a). This type of coaxial deformation causes a marked increase in the crystal aspect ratio (Fig. 6a). Since the Cardones ignimbrite was emplaced into deep valleys (van Zalinge et al. 2016b), lateral flow may also reflect downslope movement of the ignimbrite, with related laminar shear (e.g. Chapin and Lowell 1979). This explains the similarity in form to metamorphic textures, including Θ-type and φ-type mantled porpyroclasts (Fig. 7a), that are characterised by core crystals mantled by fine-grained material of the same mineral and are often observed in shear zones (Passchier and Trouw 2005).

Comparison of crystal deformation with conventional welding parameters

Finally, we interpret patterns of crystal breakage and deformation with the other indications of compaction and welding, such as bulk density and average fiamme aspect ratio. The uppermost ca. 200 m of the ignimbrite stratigraphy shows evidence of increasing welding with depth, as measured by the progressive increase in fiamme aspect ratio from two to four and the increase in bulk ignimbrite density from < 1900 to 2300 kg/m^3. In this interval, however, crystal aspect ratios are uniformly low, typically less than two. These trends indicate that compaction in the uppermost section was accommodated primarily by reduction of pore space in bulk ignimbrite and pumice clasts, without significant secondary crystal

fragmentation, rotation or deformation. At stratigraphic levels > 200 m (5 MPa), bulk ignimbrite density remains constant of ca. 2300 kg/m^3, fiamme aspect ratios increase with depth (Fig. 6a), and both fragmentation efficiency and deformation increase (Figs. 4 and 6a). Hence, we suggest that in this part of the ignimbrite stratigraphy, compaction and welding involved bubble collapse in pumice (to form fiamme) as well as secondary crystal fragmentation and associated lateral flow.

Towards the base of the ignimbrite, the average fiamme aspect ratio suddenly decreases (Fig. 6a). In holes 7 and 9, this decrease occurs in the basal 50 m. These asymmetrical fiamme flattening profiles in holes 7 and 9 indicate increased welding and compaction with increased ignimbrite loading combined with more efficient cooling at the surface relative to the base of the ignimbrite (Riehle et al. 1995). In holes 1 and 5, however, a dramatic drop in fiamme aspect ratios occurs higher above the ignimbrite base (Fig. 6a). van Zalinge et al. (2016a) related the distinct decrease in fiamme aspect ratio to a marked increase in lithic content (from << 1 to ca. 4%, Fig. 1b), and suggested that the lithic clasts could have cooled the ignimbrite, limiting fiamme flattening. This trend, however, is not seen in measurements of either bulk ignimbrite density or crystal aspect ratio. In contrast, crystals in the pumice clasts still show evidence of secondary fragmentation, which requires temperatures above the glass transition temperature. We therefore suggest an alternative interpretation for the fiamme data, which is that pumice clasts at the base of the ignimbrite were more dense (had lower overall vesicularities) and thus had less capacity for flattening during collapse. Unusually dense pumice clasts might be expected in shallower parts of the reservoir, where magma experienced the smallest pressure gradient and also by analogy with other large ignimbrite deposits, some pre-eruptive degassing (and thus the least bubble growth) (e.g. Wright et al. 2011).

Conclusions and implications

Many crystal-rich large-volume ignimbrites, including the 21.9 Ma Cardones ignimbrite in northernmost Chile, contain extensively fragmented crystals. We propose that fragmentation occurs as a two-stage process (Fig. 8). Primary crystal fragmentation records the brittle response of the magma to large stresses caused by rapid decompression (and large ΔP) associated with the eruption. Secondary fragmentation becomes prevalent at depths of ca. 200 m (ca. 5 MPa) and is associated with compaction and welding. In the Cardones, compaction is enhanced by (1) the increase of fragments per crystal caused by crystal crushing; and (2) horizontal displacement and rotation of individual crystal fragments, as recorded in the aspect ratio and extinction angles of fragmented crystals. In pumice clasts, the extra volume caused by primary crystal breakage and dilation during primary fragmentation is lost during compaction by fragment rotation, secondary

fragmentation and horizontal displacement of broken crystal pieces. These contributions of primary fragmentation to compaction have not been described previously, and may contribute to lateral spreading of thick crystal-rich ignimbrites. The overlying ignimbrite load and the duration above the glass transition temperature also control the extent of secondary fragmentation.

Density, porosity and fiamme aspect ratios are common metrics of compaction and welding (e.g. Smith 1960; Quane and Russell 2005). This study demonstrates that fragmentation and deformation of crystals in pumice (and bulk ignimbrite) provide useful additional parameters for quantifying compaction and welding. Documenting crystal fragmentation has particular implications for large-volume crystal-rich ignimbrites that have great thicknesses and contain abundant broken crystals, and is especially useful for altered ignimbrites in which the primary density and permeability might be obscured by secondary mineralisation.

References

Alidibirov M, Dingwell DB (1996) Magma fragmentation by rapid decompression. Nature 380(6570):146–148. https://doi.org/10.1038/380146a0

Allen S, McPhie J (2003) Phenocryst fragments in rhyolitic lavas and lava domes. J Volcanol Geotherm Res 126(3):263–283. https://doi.org/10.1016/S0377-0273(03)00151-3

Bachmann O, Dungan M, Lipman P (2000) Voluminous lava-like precursor to a major ash-flow tuff: low-column pyroclastic eruption of the Pagosa Peak Dacite, San Juan volcanic field, Colorado. J Volcanol Geotherm Res 98(1):153–171

Best MG, Christiansen EH (1997) Origin of broken phenocrysts in ash-flow tuffs. Geol Soc Am Bull 109(1):63–73. https://doi.org/10.1130/0016-7606(1997)109<0063:OOBPIA>2.3.CO;2

Bindeman IN (2005) Fragmentation phenomena in populations of magmatic crystals. Am Mineral 90(11–12):1801–1815. https://doi.org/10.2138/am.2005.1645

Blair DL, Mueggenburg NW, Marshall AH, Jaeger HM, Nagel SR (2001) Force distributions in three-dimensional granular assemblies: effects of packing order and interparticle friction. Phys Rev E 63(4):041304. https://doi.org/10.1103/PhysRevE.63.041304

Cashman KV, Giordano G (2014) Calderas and magma reservoirs. J Volcanol Geotherm Res 288:28–45. https://doi.org/10.1016/j.jvolgeores.2014.09.007

Cashman KV, Thornber CR, Pallister JS (2008) From dome to dust: shallow crystallization and fragmentation of conduit magma during

the 2004-2006 dome extrusion of Mount St. Helens, Washington. US Geological Survey professional paper (1750):387–413

Cashman KV, Sparks RSJ, Blundy JD (2017) Vertically extensive and unstable magmatic systems: a unified view of igneous processes. Science 355(6331):eaag3055. https://doi.org/10.1126/science.aag3055

Chapin CE, Lowell GR (1979) Primary and secondary flow structures in ash-flow tuffs of the Gribbles Run paleovalley, central Colorado. Geol Soc Am Spec Pap 180:137–154. https://doi.org/10.1130/SPE180-p137

Cordonnier B, Hess K-U, Lavallee Y, Dingwell D (2009) Rheological properties of dome lavas: case study of Unzen volcano. Earth Planet Sci Lett 279(3):263–272. https://doi.org/10.1016/j.epsl.2009.01.014

Costa A, Sparks R, Macedonio G, Melnik O (2009) Effects of wall-rock elasticity on magma flow in dykes during explosive eruptions. Earth Planet Sci Lett 288(3):455–462. https://doi.org/10.1016/j.epsl.2009.10.006

Evans JP (1988) Deformation mechanisms in granitic rocks at shallow crustal levels. J Struct Geol 10(5):437–443. https://doi.org/10.1016/0191-8141(88)90031-4

García M, Gardeweg M, Clavero J, Hérail G (2004) Arica map: Tarapacá Region, scale 1: 250,000. Serv Nac Geol Min 84:150

García M, Riquelme R, Farías M, Hérail G, Charrier R (2011) Late Miocene–Holocene canyon incision in the western Altiplano, northern Chile: tectonic or climatic forcing? J Geol Soc 168(4):1047–1060

Gardner JE, Thomas RM, Jaupart C, Tait S (1996) Fragmentation of magma during Plinian volcanic eruptions. Bull Volcanol 58(2): 144–162. https://doi.org/10.1007/s004450050132

Gottsmann J, Lavallée Y, Marti J, Aguirre-Diaz G (2009) Magma–tectonic interaction and the eruption of silicic batholiths. Earth Planet Sci Lett 284(3):426–434. https://doi.org/10.1016/j.epsl.2009.05.008

Hoover S, Cashman K, Manga M (2001) The yield strength of subliquidus basalts—experimental results. J Volcanol Geotherm Res 107(1):1–18

Huber C, Bachmann O, Dufek J (2011) Thermo-mechanical reactivation of locked crystal mushes: melting-induced internal fracturing and assimilation processes in magmas. Earth Planet Sci Lett 304:443–454

Jones TJ, McNamara K, Eychenne J, Rust AC, Cashman KV, Scheu B, Edwards R (2016) Primary and secondary fragmentation of crystal-bearing intermediate magma. J Volcanol Geotherm Res 327:70–83. https://doi.org/10.1016/j.jvolgeores.2016.06.022

Klug C, Cashman KV (1996) Permeability development in vesiculating magmas: implications for fragmentation. Bull Volcanol 58(2):87–100. https://doi.org/10.1007/s004450050128

Lavallée Y, Hess K-U, Cordonnier B, Dingwell DB (2007) Non-Newtonian rheological law for highly crystalline dome lavas. Geology 35(9):843–846. https://doi.org/10.1130/G23594A.1

Lejeune AM, Richet P (1995) Rheology of crystal-bearing silicate melts: an experimental study at high viscosities. Journal of Geophysical Research: Solid Earth 100(B3):4215–4229. https://doi.org/10.1029/94JB02985

Lindoo A, Larsen J, Cashman K, Dunn A, Neill O (2016) An experimental study of permeability development as a function of crystal-free melt viscosity. Earth Planet Sci Lett 435:45–54

Lindoo A, Larsen JF, Cashman KV, Oppenheimer J (2017) Crystal controls on permeability development and degassing in basaltic andesite magma. Geology 45(9):831–834. https://doi.org/10.1130/G39157.1

Lindsay J, Schmitt A, Trumbull R, De Silva S, Siebel W, Emmermann R (2001) Magmatic evolution of the La Pacana caldera system, Central Andes, Chile: compositional variation of two cogenetic, large-volume felsic ignimbrites. J Petrol 42(3):459–486. https://doi.org/10.1093/petrology/42.3.459

Lipman P, Dungan M, Bachmann O (1997) Comagmatic granophyric granite in the Fish Canyon Tuff, Colorado: implications for magma-chamber processes during a large ash-flow eruption. Geology 25(10):915–918

Liu AJ, Nagel SR (2010) The jamming transition and the marginally jammed solid. Annu Rev Condens Matter Phys 1(1):347–369. https://doi.org/10.1146/annurev-conmatphys-070909-104045

Mueller S, Scheu B, Spieler O, Dingwell DB (2008) Permeability control on magma fragmentation. Geology 36(5):399–402. https://doi.org/10.1130/G24605A.1

Mueth DM, Jaeger HM, Nagel SR (1998) Force distribution in a granular medium. Phys Rev E 57(3):3164–3169. https://doi.org/10.1103/PhysRevE.57.3164

Oppenheimer J, Rust AC, Cashman KV, Sandnes B (2015) Gas migration regimes and outgassing in particle-rich suspensions. Front Phys 3:60

Pamukcu AS, Gualda GA, Anderson AT (2012) Crystallization stages of the Bishop Tuff magma body recorded in crystal textures in pumice clasts. J Petrol 53(3):589–609. https://doi.org/10.1093/petrology/egr072

Papale P (1999) Strain-induced magma fragmentation in explosive eruptions. Nature 397(6718):425–428. https://doi.org/10.1038/17109

Passchier C, Trouw R (2005) Microtectonics, 366 pp. Springer, Berlin

Paterson SR, Fowler TK, Schmidt KL, Yoshinobu AS, Yuan ES, Miller RB (1998) Interpreting magmatic fabric patterns in plutons. Lithos 44(1):53–82. https://doi.org/10.1016/S0024-4937(98)00022-X

Peterson DW (1979) Significance of the flattening of pumice fragments in ash-flow tuffs. Geol Soc Am Spec Pap 180:195–204. https://doi.org/10.1130/SPE180-p195

Petford N (2003) Rheology of granitic magmas during ascent and emplacement. Annu Rev Earth Planet Sci 31(1):399–427. https://doi.org/10.1146/annurev.earth.31.100901.141352

Polacci M, Papale P, Rosi M (2001) Textural heterogeneities in pumices from the climactic eruption of Mount Pinatubo, 15 June 1991, and implications for magma ascent dynamics. Bull Volcanol 63(2–3):83–97

Quane SL, Russell JK (2005) Ranking welding intensity in pyroclastic deposits. Bull Volcanol 67(2):129–143. https://doi.org/10.1007/s00445-004-0367-5

Rasband W (1997) ImageJ. US National Institutes of Health, Bethesda

Riehle J, Miller T, Bailey R (1995) Cooling, degassing and compaction of rhyolitic ash flow tuffs: a computational model. Bull Volcanol 57(5): 319–336

Rosi M, Landi P, Polacci M, Di Muro A, Zandomeneghi D (2004) Role of conduit shear on ascent of the crystal-rich magma feeding the 800-year-BP Plinian eruption of Quilotoa Volcano (Ecuador). Bull Volcanol 66(4):307–321

Rushmer T (1995) An experimental deformation study of partially molten amphibolite: application to low-melt fraction segregation. Journal of Geophysical Research: Solid Earth 100(B8):15681–15695. https://doi.org/10.1029/95JB00077

Rust A, Cashman K (2011) Permeability controls on expansion and size distributions of pyroclasts. J Geophys Res Solid Earth 116(B11). https://doi.org/10.1029/2011JB008494

Rutter E, Neumann D (1995) Experimental deformation of partially molten Westerly granite under fluid-absent conditions, with implications for the extraction of granitic magmas. Journal of Geophysical Research: Solid Earth 100(B8):15697–15715. https://doi.org/10.1029/94JB03388

Saar MO, Manga M, Cashman KV, Fremouw S (2001) Numerical models of the onset of yield strength in crystal–melt suspensions. Earth Planet Sci Lett 187(3):367–379. https://doi.org/10.1016/S0012-821X(01)00289-8

Smith RL (1960) Zones and zonal variations in welded ash flows. USGS Prof Pap 354-F:149–159

Sparks RSJ (1978) The dynamics of bubble formation and growth in magmas: a review and analysis. J Volcanol Geotherm Res 3(1–2): 1–37. https://doi.org/10.1016/0377-0273(78)90002-1

Sparks R, Barclay J, Jaupart C, Mader H, Phillips J (1994) Physical aspects of magmatic degassing I. Experimental and theoretical constraints on vesiculation. MSA Rev Mineral 30:413–443

Sparks R, Tait S, Yanev Y (1999) Dense welding caused by volatile resorption. J Geol Soc 156(2):217–225. https://doi.org/10.1144/gsjgs.156.2.0217

Spieler O, Kennedy B, Kueppers U, Dingwell DB, Scheu B, Taddeucci J (2004) The fragmentation threshold of pyroclastic rocks. Earth Planet Sci Lett 226(1):139–148. https://doi.org/10.1016/j.epsl.2004.07.016

Tait S (1992) Selective preservation of melt inclusions in igneous phenocrysts. Am Mineral 77(1–2):146–155

Van der Molen I, Paterson M (1979) Experimental deformation of partially-melted granite. Contrib Mineral Petrol 70(3):299–318. https://doi.org/10.1007/BF00375359

van Zalinge ME, Sparks RSJ, Cooper FJ, Condon DJ (2016a) Early Miocene large-volume ignimbrites of the Oxaya Formation, Central Andes. J Geol Soc 173:716–733 jgs2015–2123

van Zalinge ME, Sparks RSJ, Evenstar LA, Cooper FJ, Aslin J, Condon DJ (2016b) Using ignimbrites to quantify structural relief growth and understand deformation processes: implications for the development of the Western Andean Slope, northernmost Chile. Lithosphere L593:591

Van Zalinge ME, Sparks RSJ, Blundy JD (2017) Petrogenesis of the large-volume Cardones ignimbrite, Chile; development and destabilisation of a complex magma-mush system. J Petrol. https://doi.org/10.1093/petrology/egx079

Walsh SD, Saar MO (2008) Numerical models of stiffness and yield stress growth in crystal-melt suspensions. Earth Planet Sci Lett 267(1):32–44. https://doi.org/10.1016/j.epsl.2007.11.028

Willcock M, Bargossi G, Weinberg R, Gasparotto G, Cas R, Giordano G, Marocchi M (2015) A complex magma reservoir system for a large volume intra-to extra-caldera ignimbrite: mineralogical and chemical architecture of the VEI8, Permian Ora ignimbrite (Italy). J Volcanol Geotherm Res 306:17–40

Williamson B, Di Muro A, Horwell C, Spieler O, Llewellin E (2010) Injection of vesicular magma into an andesitic dome at the effusive–explosive transition. Earth Planet Sci Lett 295(1):83–90

Wörner G, Hammerschmidt K, Henjes-Kunst F, Lezaun J, Wilke H (2000) Geochronology (40Ar/39Ar, K-Ar and He-exposure ages) of Cenozoic magmatic rocks from Northern Chile (18-22° S): implications for magmatism and tectonic evolution of the central Andes. Rev Geol Chile 27(2):205–240

Wright HM, Cashman KV (2014) Compaction and gas loss in welded pyroclastic deposits as revealed by porosity, permeability, and electrical conductivity measurements of the Shevlin Park Tuff. Geol Soc Am Bull 126(1–2):234–247. https://doi.org/10.1130/B30668.1

Wright HM, Weinberg RF (2009) Strain localization in vesicular magma: implications for rheology and fragmentation. Geology 37(11):1023–1026. https://doi.org/10.1130/G30199A.1

Wright HM, Folkes CB, Cas RA, Cashman KV (2011) Heterogeneous pumice populations in the 2.08-Ma Cerro Galán Ignimbrite: implications for magma recharge and ascent preceding a large-volume silicic eruption. Bull Volcanol 73(10):1513–1533. https://doi.org/10.1007/s00445-011-0525-5

Zhang Y (1998) Mechanical and phase equilibria in inclusion–host systems. Earth Planet Sci Lett 157(3):209–222. https://doi.org/10.1016/S0012-821X(98)00036-3